Tolerating B_1^+-inhomogeneity in MP2RAGE-based R_1-mapping by calculating second contrast that permits previously problematic sequence parameters

Lenno Ruijters[a,†], Torben Ellegaard Lund[a], Mads Sloth Vinding[a]

[a] Center of Functionally Integrative Neuroscience, Department of Clinical Medicine, Aarhus University, Aarhus, Denmark

[†] Corresponding author: Lenno Ruijters, au710840@uni.au.dk

ORCID:

Lenno Ruijters: 0009-0001-8207-3830

Torben E. Lund: 0000-0002-9002-4676

Mads S. Vinding: 0000-0002-0149-583X

SUBMITTED TO MAGNETIC RESONANCE IN MEDICINE.

Abstract:

Purpose: Regarding robust R_1-mapping, the goal of the present paper is twofold. First, to verify that non-bijective mapping in MP2RAGE imaging can be resolved through a 2D look-up table approach. Second, that the expanded parameter space from this can be used to improve B_1^+-inhomogeneity tolerance without other prerequisites.

Theory and Methods: By deriving a second contrast from the magnitude images of the MP2RAGE acquisition, ambiguities in the original unified MP2RAGE image can be resolved. Such ambiguities may occur when sequences are optimised, e.g., for higher B_1^+-inhomogeneity tolerance. A 2D look up procedure can then be used to derive accurate R_1-maps.

Results: We acquired two sets of images, one according to a standard MP2RAGE protocol, and one optimised for B_1^+-inhomogeneity contrast, the latter resulting in non-bijective mapping. For each protocol, we acquired three images, using different excitation pulse amplitude scalings to magnify the B_1^+-inhomogeneities between images. The R_1-maps resulting from the B_1^+-optimised sequence showed greatly reduced B_1^+-effects across images, while these maps could only successfully be derived by 2D look-up approach.

Conclusion: We show that it is indeed possible to improve B_1^+-inhomogeneity tolerance in MP2RAGE through sequence parameter settings, while still successfully estimating the R_1-map with a 2D look-up table approach. The increased parameter space enabled by the 2D look-up approach may further be used to adjust MP2RAGE acquisitions for improved scan times or improved contrasts.

1. Introduction

If R_1-mapping is to be used in making subject-specific, in-vivo, detailed maps of human cortical structures (building on Refs.[1–3]), then it is important that R_1-changes reflect variations in myelo-architecture rather than contaminations from artefacts. To map structurally distinct cortical areas beyond primary sensory tissue (e.g. Refs.[1–3]), i.e. whole-brain, highly refined images are required. In order to detect subtle variations, these images need to be detailed and reliable, i.e. have high resolution and minimal artefact contributions. One prominent source of artefacts is B_1^+-inhomogeneity, which modulates the nominal flip angle, and consequently the measured signal. Three factors that affect the size of B_1^+-effects are B_0, readout train length, and T_R. The result is that, as we strive for higher resolutions, B_1^+-artefacts increasingly counteract the benefits of the increased spatial detail. Methodological strategies are necessary to limit the loss in R_1-specificty as increased resolutions are achieved.

MP2RAGE is a T_1-weighted MRI-sequence that produces quantitative maps, while simultaneously mitigating the effects of B_1-inhomogeneities[4]. By acquiring two Rapid Gradient Echos, and by combining these in post-processing into a unified MP2RAGE image, it is possible to eliminate T_2*, B_0 and B_1^- effects. Calibrating sequence parameters, like the flip angles or inversion times, further make it possible to minimize the B_1^+-effects. Since unified MP2RAGE images are quantitative, the values in these images can be derived from T_1 and the sequence parameters. Via Bloch simulations, a mapping can be derived between T_1 and unified MP2RAGE values. If the mapping is bijective (i.e. one-to-one), then each MP2RAGE value can be uniquely associated with a T_1-value[5]. However, parameters with desirable features, including improved tolerance to B_1^+-inhomogeneities, but also high within- or between-tissue contrast or faster scanning times, may produce mappings that are non-bijective. In such cases, tissues in the R_1-maps are mislabelled and a different strategy is required to successfully derive R_1-maps.

In this paper, we investigate the possibility of mitigating B_1^+-effects with modified sequence parameters, by tackling the challenge of non-bijective mappings between unified MP2RAGE values and T_1. To this end, we introduce a new strategy able to derive R_1-maps from MP2RAGE acquisitions with non-bijective mappings. The present R_1-mapping utilises a secondary contrast, derived from the MP2RAGE acquisition based on the ratio between the difference and the sum of the magnitude of the two gradient echo images (Difference-Sum-Ratio; DSR). Similar to the unified MP2RAGE image, effects related to T_2*, B_0 and B_1^- are cancelled out in the DSR image. Additionally, the DSR-contrast is suitable for disambiguation of unified

MP2RAGE values. Consequently, accurate R_1-maps can be determined for non-bijective mappings, as is the case in sequences highly tolerant of B_1^+-inhomogeneity, for example.

2. Theory

Quantitative T_1-weighted images are derived from the MP2RAGE acquisition by combining the images acquired from each echo (I_1, I_2) voxel by voxel into a unified image (I_{UNI}):

$$I_{UNI} = \Re\left(\frac{I_1^* \cdot I_2}{|I_1|^2 + |I_2|^2}\right). \qquad [1]$$

In the case where nuisance factors contribute equally to I_1 and I_2, these effects cancel out in I_{UNI}. By nature of Eq. (1), I_{UNI}-values are bound between -0.5 and +0.5, and exactly equal to ±0.5, when $I_1 = \pm I_2$. Because these values are quantitative, I_{UNI}-values can be derived from T_1. In standard implementations, I_{UNI} is mapped to T_1-values by means of a 1-dimensional look-up table (1D-LUT). The mapping can also be visualised as a transfer curve (see Fig 1). A bijective relationship between UNI and T_1 is required for the 1D-LUT procedure to be applicable. This is achieved by careful selection of sequence parameters (Fig 1a)[4]. By scaling the flip angles, the effects of B_1^+-inhomogeneity on estimated R_1-values can also be derived and visualised as separate transfer curves.

It is possible to select sequence parameters where the corresponding transfer curve results in less dependency on B_1^+-variations (see Fig 1b). However, such parameters may lead to a mapping which is non-bijective within the T_1-window-of-interest. At that point the 1D-LUT method fails, because T_1-values from two different tissue types (e.g. grey matter (GM) and cerebrospinal fluid (CSF)) map to the same I_{UNI}-value. Non-bijection in the mapping occurs when $I_1 = \pm I_2$. For standard sequence parameters, non-bijection will typically occur for long T_1s (≈5s), leading to large T_1-variance within CSF, which is largely unproblematic. For mappings where the non-bijection occurs at relatively low T_1-values (like in Fig 1b), a solution is needed.

By introducing a second, distinct contrast that is derived from the MP2RAGE-images, I_1 and I_2, we are able to solve ambiguities in non-bijective mappings, and accurately estimate the R_1-values. This second contrast can be defined in a number of ways. We settled on a combination of the magnitudes of I_1 and I_2, because these magnitude images are readily available in standard setups. Similar to I_{UNI}, we further want this second contrast to be quantitative and tolerant to magnetic field inhomogeneities. The ratio between the difference of the first and second

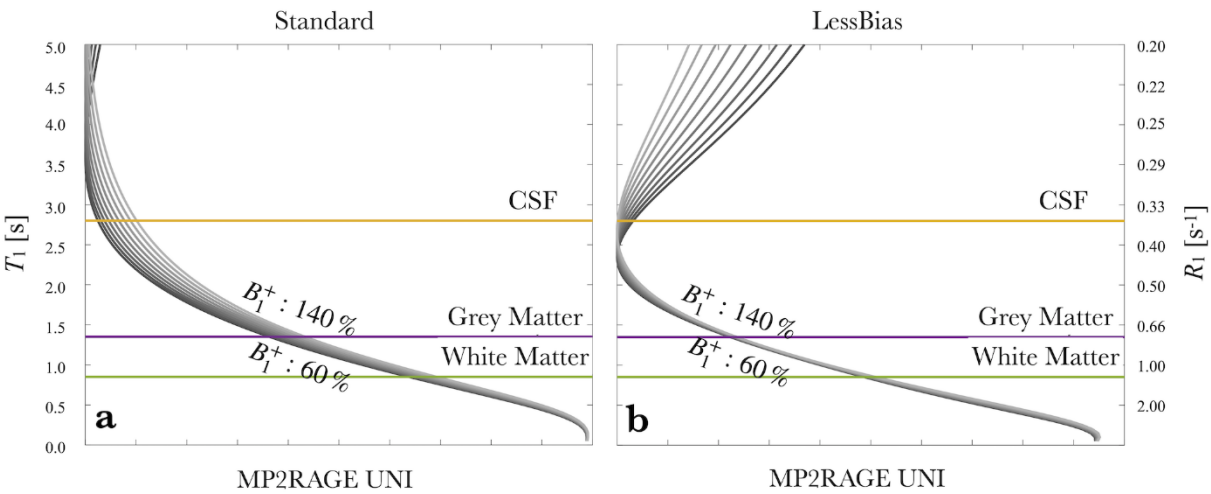

Figure 1: The MP2RAGE-to-T_1 transfer curves for the Standard (a) and LessBias (b) protocols, with corresponding R_1-values on the right axis. The Standard protocol, (a), is more sensitive to B_1^+-inhomogeneities than the LessBias protocol, (b), which is almost insensitive to B_1^+-variations in the order of +/- 40%. Within the range of T_1-values from 0 to 5 s the Standard protocol, (a), has a near-bijective relationship between the MP2RAGE UNI values and T_1; this is not the case for the LessBias protocol, (b), where within the T_1-window, there are ambiguous UNI values.

magnitude values, and the sum of them (Difference-Sum-Ratio, I_{DSR}) satisfies these requirements:

$$I_{DSR} = \frac{|I_1|-|I_2|}{2(|I_1|+|I_2|)} \,. \qquad [2]$$

The factor of 2 in the denominator ensures that the I_{DSR}-values fall within the same range as the I_{UNI}-values (i.e. between -0.5 and 0.5). As I_{DSR} equals ±0.5 when either $|I_1|$ or $|I_2|$ is 0, and I_{DSR} equals 0 where $|I_1|=|I_2|$, the I_{DSR} contrast is indeed distinct from I_{UNI}, where this behaviour is inverted. Similar to I_{UNI}, nuisance factors contributing equally to $|I_1|$ and $|I_2|$ are cancelled out in I_{DSR}.

The disambiguation of the non-bijective mapping is performed by using a 2D-lookup table (2D-LUT), connecting a pair of (I_{UNI}, I_{DSR})-values to their corresponding T_1-value. In its simplest implementation, the 2D-LUT procedure compares the Euclidean distance between measured and theoretical value-pairs to obtain the T_1-value (here `pdist2` in MATLAB; The MathWorks, Inc., Natick, MA); this is illustrated in Figure 2. To ensure that the T_1-estimation is driven by

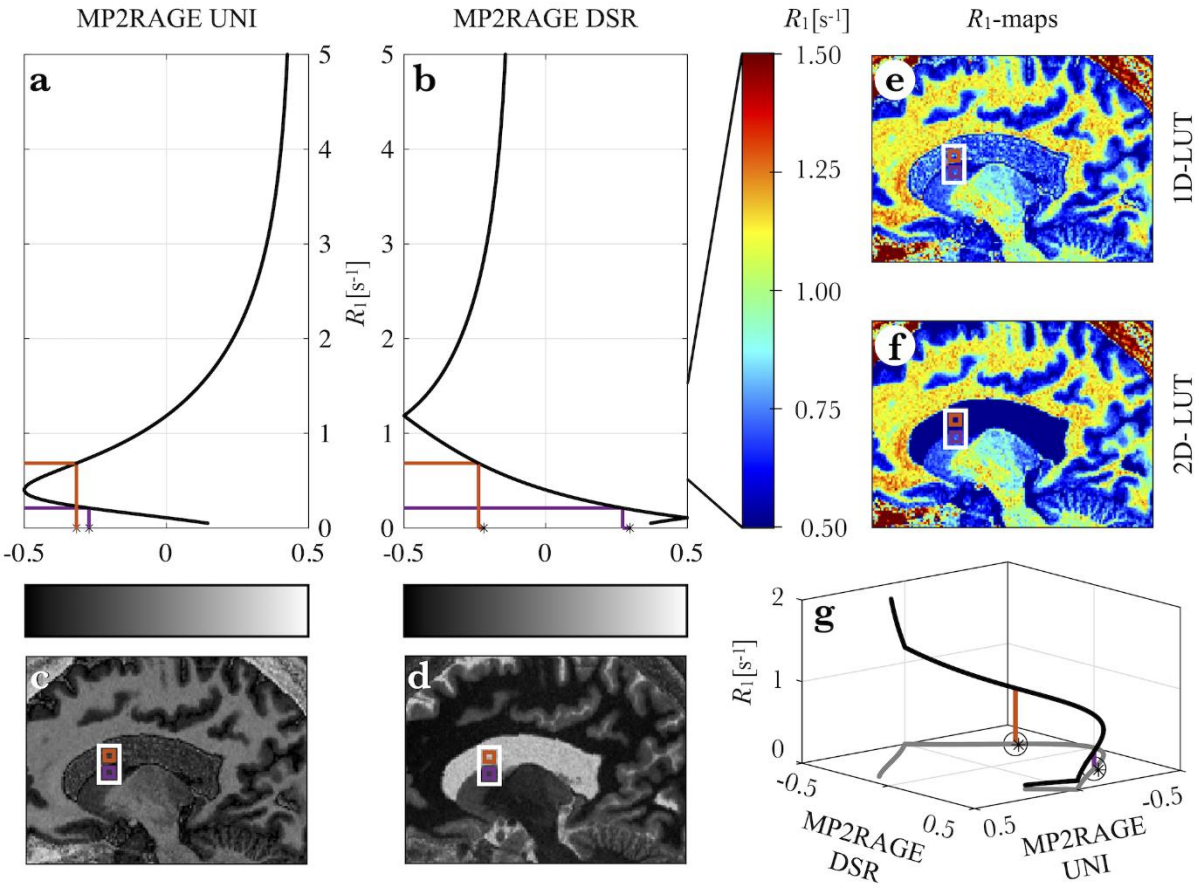

Figure 2: (a,b) 1D transfer curves for the MP2RAGE UNI (c) and DSR (d) of the LessBias protocol, respectively. (e,f) Resulting 1D- and 2D-LUT R_1-maps, respectively. (g) 2D transfer curve between MP2RAGE UNI, DSR and R_1. The MP2RAGE DSR, (d), can be used to disentangle the ambiguous relationship between the MP2RAGE UNI image, (c), and the R_1-value, (a,b). The method is illustrated for CSF (purple) and deep GM (orange) voxels with MP2RAGE UNI values close to each other. By Identifying the MP2RAGE values in both the MP2RAGE UNI image and the MP2RAGE DSR image, a unique R_1-value can be assigned to each voxel using a 2D-LUT (f), but not a 1D-LUT (e). (g) Illustrates that the mapping is unambiguous in the full MP2RAGE UNI, DSR, R_1-space.

the UNI-values, as is the case for 1D-LUT, a larger weight can be applied to I_{UNI} by equally scaling the measured and theoretical I_{UNI}-values.

3. Methods

The purpose of the present study is twofold: first, to verify that R_1-mapping can be performed successfully in expanded sequence parameter space, by resolving non-bijective mapping through 2D-LUT; and second, that from this expanded parameter space, parameters can be selected that result in R_1-maps that tolerate B_1^+-inhomogeneities to an extent unseen without non-bijective mapping. To demonstrate our proposed method, we acquired experimental data in a single session from one of the authors (LR) on a 3T Siemens PrismaFit system (Siemens Healthineers, Erlangen, Germany), using a 32-channel receive-only head coil. Images were acquired with our standard protocol (Standard) representing the default configuration of the host site, and a new protocol (LessBias) with improved tolerance to B_1^+-inhomogeneities in the

final R_1-maps: 1) Standard: $T_{R,MP2RAGE}$=5s, $T_{R,FLASH}$=7.18ms, α_1/α_2=4°/5°, $T_{I,1}/T_{I,2}$=700ms/2500ms; 2) LessBias: $T_{R,MP2RAGE}$=5s, $T_{R,FLASH}$=7.18ms, α_1/α_2=3°/5°, $T_{I,1}/T_{I,2}$=500ms/1900ms. In both cases, a single acquisition of 11:20 minutes with a 215.6×172.8×230mm field of view (Anterior-Posterior/Left-Right/Superior-Inferior; phase/slice/read), a grid size 256×192×240, i.e. 0.9mm³ isotropic voxels, partial Fourier=6/8, and 2xGRAPPA[6]. Additionally, fat navigator-based motion correction was applied[7,8]. To systematically amplify B_1^+-inhomogeneity, we modified the excitation pulse amplitude ("SRFExcit" in the scan card; Supplementary Figure S1). Each protocol was acquired three times, with a SRFExcit setting at 60%, 100% and 140% of the reference voltage across acquisitions, which reflect the range of B_1^+-inhomogeneities seen at 7T[4].

Following motion correction[7,8], the anterior (AC) and posterior (PC) commissure were identified on the Standard image acquired with no flip angle alterations. Next all images from both the Standard and the LessBias were reoriented accordingly, to obtain a near AC-PC space orientation in all acquisitions. For each acquisition an R_1-map was now created using a 1D-LUT[5] for the Standard acquisitions and the newly introduced 2D-LUT method for the LessBias acquisitions.

The 2D-LUT R_1-mapping was performed by using a step-size of ΔR_1=0.001s^{-1} and a minimum $R_1 \leq 0.05$s^{-1}. We opted for equidistant R_1-spacing rather than equidistant T_1-spacing, to better capture variations in the WM-GM range. In order to most directly compare the results of the 1D-LUT R_1-mapping approach and the 2D-LUT approach introduced here, we applied a strong 100:1 weight ratio between I_{UNI} and I_{DSR} before calculating the Euclidian distance. This ensured that R_1-values were assigned on the basis of the UNI values, with DSR values used primarily for disambiguation.

The R_1-maps were then segmented using SPM12 r7711[9,10], and from the segmented images two masked R_1-maps were created. The first masked image was constructed from a 1-step eroded brain mask containing voxels, where the sum of posterior probabilities for CSF, GM and WM exceeded 0.2. The second was constructed similarly, but also for skull and soft tissue voxels. The brain-only-masked R_1-maps were co-registered to the Standard acquisition with an unscaled excitation pulse amplitude, and the estimated registrations were applied to all images within each protocol. The brain-masked, co-registered R_1-maps were used to calculate the mean and standard deviation images between the different excitation pulse amplitude scalings within each protocol (Standard and LessBias). These mean and standard deviation maps were used to

assess the standard deviation within each tissue type. While this approach is suited to evaluate the effects of B_1^+-inhomogeneity in CSF and WM, the effects within GM are better visualised on a central GM surface.

To construct the central GM surfaces, we used CAT12 r2560[11–14] to segment the head-masked, co-registered R_1-maps and followed the iso-volume approach[15,16]. By sampling each R_1-map on their corresponding central GM surface and projecting out the local curvature[1], we obtained curvature-corrected central GM R_1-surfaces for each of the three excitation pulse amplitude scalings within each protocol. Prior to curvature correction, both curvature- and R_1-surfaces were resampled to the FreeSurfer template surface in CAT12, and 2D-smoothed with a Gaussian kernel (FWHM 6mm). From these surfaces, we calculated the standard deviation between the different excitation pulse amplitude scalings, within each protocol. Finally, the curvature-corrected R_1-values and their standard deviations were visualised on an inflated GM template surface.

4. Results

The SNR is highly comparable between the two sequences, Standard and LessBias, for a nominal excitation flip angle, i.e., SRFExcit of 100%. When SNR is defined as the maximum intensity value across $|I_1|$ and $|I_2|$ divided by the mean intensity value of the background of $|I_1|$, $SNR_{Standard} \approx 75$ and $SNR_{LessBias} \approx 71$.

Figure 1 shows the theoretical transfer curves of Standard (1a) and LessBias (1b), the latter being non-bijective within the T_1-window-of-interest (0-5s), with the fold occurring at approximately T_1=2.5s. Additionally, the estimated B_1^+-inhomogeneity tolerance in the GM and white matter (WM) range for LessBias is strongly improved compared to Standard. Figure 2 visualises the 2D-LUT approach. Figure 2e shows how the 1D-LUT approach fails as it gives

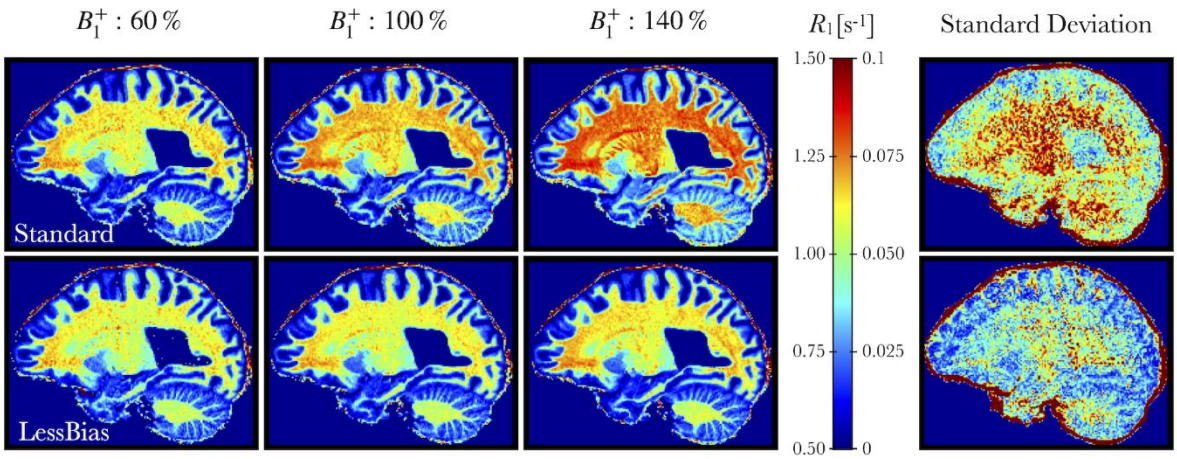

Figure 3: (top) Images from the Standard protocol. (bottom) Images from the LessBias protocol. By scaling the excitation pulse amplitude to 60%, 100% and 140%, it is possible to visualise the benefit of the LessBias protocol. As can be seen from both the individual acquisitions and the standard deviation image, the LessBias protocol does indeed, as predicted from Figure 1, demonstrate robustness to deviations from the nominal B_1^+. From the standard deviation images, it can be observed that LessBias provides a reduced standard deviation by roughly a factor of two for GM and WM, at the cost of a slightly increased standard deviation for CSF, compared to the Standard protocol.

rise to ambiguous R_1-values across CSF (purple square) and GM (orange square). Figure 2f shows that the non-bijective mapping can be resolved with a 2D-LUT.

In Figures 3, 4 and 5, the results of artificially amplifying the B_1^+-inhomogeneities are outlined. In Figure 3, substantial WM R_1-variation is seen across the different levels of B_1^+-amplification using the Standard protocol. In contrast, using the LessBias protocol combined with 2D-LUT, consistent WM R_1-values are obtained across B_1^+-amplifications. We see that the standard deviations across amplifications in WM are reduced by a factor of 2 for the LessBias protocol, see also Supplementary Figure S2.

In Figures 4 and 5, the variability in R_1-values is displayed on central GM surfaces. For the Standard protocol, Figure 4a (left) shows substantial variation in R_1-values when displayed with identical windowing across images. When the images are windowed to their individual 5th-95th percentile ranges (4a, right), then this variation is obscured. For the standard deviation, we see that the 95th percentile ranges to ≈0.05s^{-1} (Fig 4b). Nonetheless, when windowed to the 5th-95th percentile range of each individual image, increased R_1-values are seen in previously reported, highly myelinated areas (e.g. V1/V5-MT+/M1/S1/A1[1–3]), as expected.

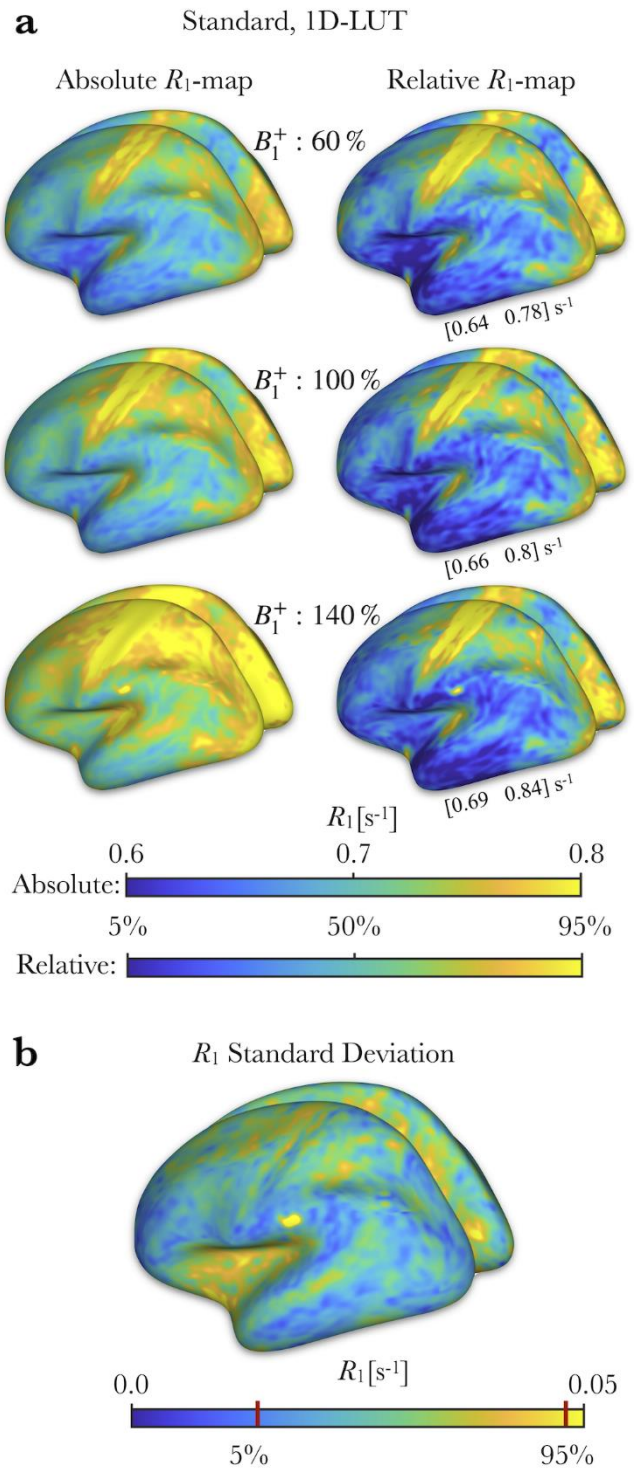

Figure 4: GM surface R_1-maps for the Standard protocol images estimated using the 1D-LUT approach. (a, left) GM surfaces with uniform windowing across images (0.6 - 0.8 s^{-1}). (a, right) GM surfaces with windowing set to the 5th to 95th percentile range of the individual images (actual range shown below each surface). (b) GM surface map of the standard deviation. Red ticks indicate the 5th and 95th percentiles of the standard deviations. Images in (a, left) and (b) indicate that B_1^+-variations substantially affect the absolute R_1-maps, while this variability is obscured in the relative R_1-maps (a, right). Increased R_1-values are observed in expected regions (V1, M1, S1, A1, and possibly V5), and especially consistent across the relative R_1-maps (a).

For the LessBias protocol (Figure 5), not only are the images windowed to the 5th-95th percentile range (5a, right) consistent across amplifications, we also see that when using identical windowing across images, this consistency is maintained (5a, left). Furthermore, when looking at the standard deviation, the 95th percentile is reduced roughly by a factor of three relative to the Standard protocol (5b). Similar to the Standard protocol, we see that when images are windowed to the 5th-95th percentile range, the previously mentioned highly myelinated areas can be identified.

5. Discussion

By utilising a 2D-LUT approach for R_1-mapping, we have expanded the MP2RAGE sequence parameter space, which enabled us to further refine the features of the MP2RAGE sequence. In this paper, we focussed on the potential for improving tolerance to B_1^+-inhomogeneity, since these artefacts impede the path towards ultrahigh resolution. Given the push for higher field strengths[17,18], driven by this desire for higher resolutions, the problem of B_1^+-inhomogeneity intolerance will only become more pressing. To introduce

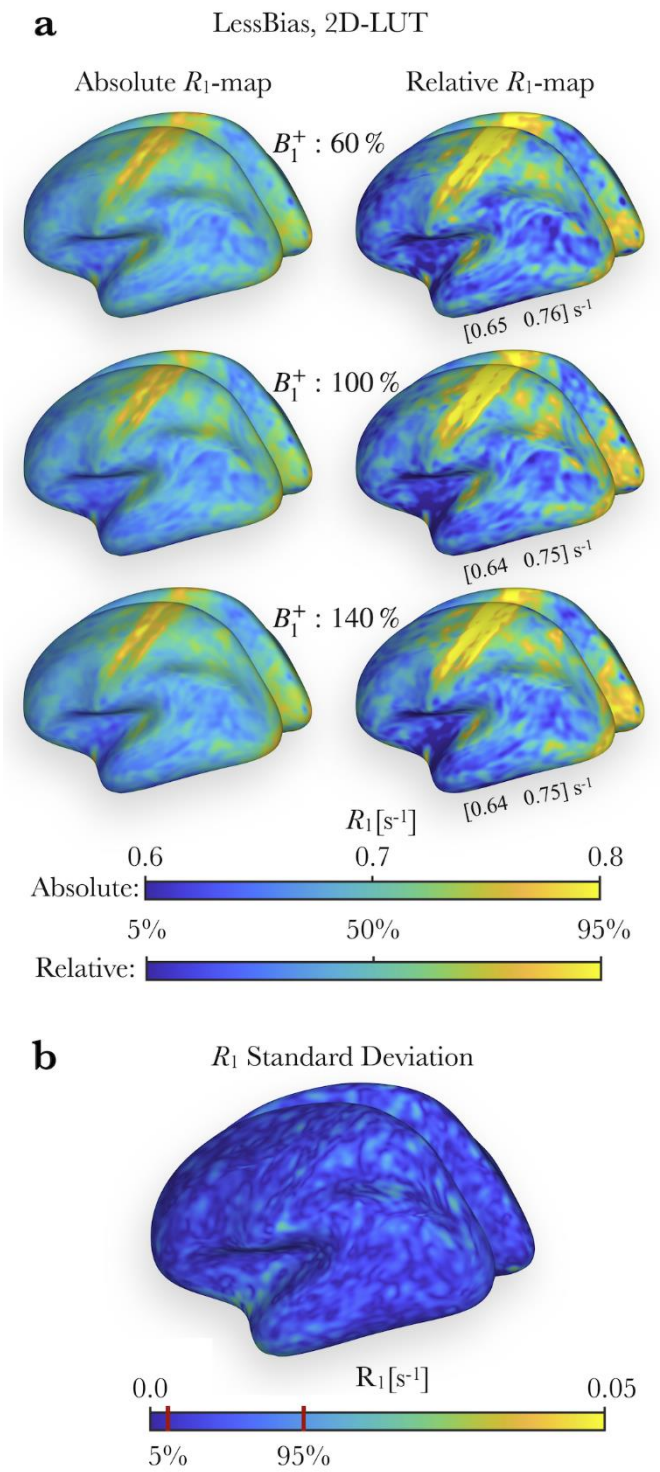

Figure 5: GM surface R_1-maps for the LessBias protocol images estimated using the 2D-LUT approach. (a, left) GM surfaces with uniform windowing across images (0.6 - 0.8 s^{-1}). (a, right) GM surfaces with windowing set to the 5th to 95th percentile range of the individual images (actual range shown below each surface). (b) GM surface map of the standard deviation. Red ticks indicate the 5th and 95th percentiles of the standard deviations. Across all images, B_1^+-variations have a limited effect, including across the relative R_1-maps (see Figure 4a, right for comparison). When windowing is set to the 5th to 95th percentile of the individual image (a, right) increased R_1-values are observed in expected regions (V1, M1, S1, A1, and possibly V5).

levels of B_1^+-inhomogeneities similar to those seen at 7T, we manipulated the amplitude of the excitation pulse. We showed that it is indeed possible to achieve greatly improved B_1^+-inhomogeneity tolerance with minimal SNR compromise. Using the adjusted sequence parameters in combination with a 2D-LUT mapping approach, we reduced the standard deviation of WM R_1-values by a factor of 2, and GM R_1-values by a factor of 3, without extending the acquisition time.

There are alternative methods that correct for B_1^+ either at the acquisition stage (e.g. pTx[19,20]) or in post-processing[21–23]. These strategies and the one proposed here can be used in concert with one another, in which case our method will likely improve robustness overall. Whether or not MP2RAGE is acquired in combination with e.g. B_1^+-mapping-based approaches, we have not come across any immediate downsides of utilising our method, given that the potential benefits come at virtually no cost compared to standard MP2RAGE applications.

On its own, our method provides B_1^+-inhomogeneity tolerance at the voxel-level without modified sequences or increased scan times. B_1^+-inhomogeneity correction with such efficiency at this resolution is to our knowledge

unprecedented, irrespective of whether compared to methods at the acquisition or post-processing stage. Time otherwise needed for such high resolution B_1^+-inhomogeneity corrections can instead be utilised to improve throughput or resolution of R_1-images. Given that the approach proposed here is agnostic to hardware setup and availability of secondary sequences, we anticipate that our method can be implemented to tackle the challenges of cross-site collaborations[24], to a larger extent than alternative methods.

Recent developments with synthetic T_1-contrasts showed that through a sufficiently accurate T_1-map, different T_1-weighted contrasts can be derived in post-processing, and that this can be used to optimise scan times[25]. When relying on synthetic MRI, the contrast of the original acquisition can be arbitrary, as long as the T_1-mapping succeeds. This means that I_{UNI} no longer needs to be visually interpretable and permits non-bijection. Consequently, further optimisations for improved B_1^+-inhomogeneity tolerance, SNR, and/or acquisition times may be possible in the wider sequence parameter space. Desired (visually interpretable) contrasts can then be computed from the resultant T_1-maps.

Other implementations for non-bijective transfer curves may be for specialised uses (e.g. Ref.[26]). Such cases may require sequence parameters that come with increased CNR in or across specific tissues (e.g. simultaneous brain and cervical spinal cord imaging). Reducing the slope of the transfer curve will lead to increased contrast between tissues in I_{UNI}, but will also lead to non-bijective transfer curves when the slope drops below a certain threshold. When such sequences are desired, the 2D-LUT R_1-mapping introduced here will still be able to derive accurate R_1-maps from the data. Through additional post-processing steps, the high contrast from the original images could be extracted, while the R_1-map serves as a reference.

The focus of the present study was on using 2D-LUT R_1-mapping to optimise for B_1^+-inhomogeneity tolerance. Other implementations could include faster sequences, or sequences with selective contrast. A common challenge for both 1D- and 2D-LUT procedures is R_1-nulling, which occurs for R_1-values where the transfer curves folds, see Supplementary Figure S2. Generally, this can be handled if sequence parameters are chosen such that the fold(s) happen(s) distant to R_1-values in the tissues of interest. However, for certain purposes, like selective contrast, it may be difficult to avoid R_1-nulling in critical R_1s. More sophisticated algorithms may prove equipped to handle such data, and are under investigation.

6. Conclusions

With a 2D-LUT R_1-mapping approach, we were able to open up the usable MP2RAGE acquisition parameter space, which can impart non-bijective MP2RAGE-to-T_1 transfer curves. This increased freedom was used to address B_1^+-inhomogeneity without additional hardware or data than what the current MP2RAGE sequence inherently provides. Compared to typical MP2RAGE acquisition parameters, we saw greatly reduced variability across GM and WM R_1-values with B_1^+-variations (±40%) mimicking those seen at 7T. While this paper focussed on improving B_1^+-inhomogeneity tolerance, this 2D-LUT mapping may also enable the use of sequences that provide contrast or scan times previously unseen in MP2RAGE.

Code availability

Code and example dataset are available at https://github.com/torbenelund/2D-lookup-tools-for-MP2RAGE.

Acknowledgements

Funding: MSV, Lundbeck Foundation; LR, Familien Andresens selskab til fremme af medicinsk forskning. Thanks to Daniel Gallichan for providing access to FatNavs-MP2RAGE sequence.

References

1. Lutti A, Dick F, Sereno MI, Weiskopf N. Using high-resolution quantitative mapping of R1 as an index of cortical myelination. *NeuroImage*. 2014;93:176-188. doi:10.1016/j.neuroimage.2013.06.005

2. Dick F, Taylor Tierney A, Lutti A, Josephs O, Sereno MI, Weiskopf N. In Vivo Functional and Myeloarchitectonic Mapping of Human Primary Auditory Areas. *J Neurosci*. 2012;32(46):16095-16105. doi:10.1523/JNEUROSCI.1712-12.2012

3. Glasser MF, Van Essen DC. Mapping Human Cortical Areas *In Vivo* Based on Myelin Content as Revealed by T1- and T2-Weighted MRI. *J Neurosci*. 2011;31(32):11597-11616. doi:10.1523/JNEUROSCI.2180-11.2011

4. Marques JP, Kober T, Krueger G, van der Zwaag W, Van de Moortele PF, Gruetter R. MP2RAGE, a self bias-field corrected sequence for improved segmentation and T1-

mapping at high field. *NeuroImage*. 2010;49(2):1271-1281. doi:10.1016/j.neuroimage.2009.10.002

5. Marques JP. MP2RAGE scripts. https://github.com/JosePMarques/MP2RAGE-related-scripts. Accessed April 5, 2024.

6. Griswold MA, Jakob PM, Heidemann RM, et al. Generalized autocalibrating partially parallel acquisitions (GRAPPA). *Magnetic Resonance in Medicine*. 2002;47(6):1202-1210. doi:10.1002/mrm.10171

7. Gallichan D, Marques JP, Gruetter R. Retrospective correction of involuntary microscopic head movement using highly accelerated fat image navigators (3D FatNavs) at 7T. *Magnetic Resonance in Medicine*. 2016;75(3):1030-1039. doi:10.1002/mrm.25670

8. Gallichan D. Retro-MoCo-Box. https://github.com/dgallichan/retroMoCoBox. Accessed April 5, 2024.

9. FRISTON K, ASHBURNER J, KIEBEL S, NICHOLS T, PENNY W, eds. In: *Statistical Parametric Mapping*. London: Academic Press; 2007:625-647. doi:10.1016/B978-012372560-8/50050-4

10. The University College London. SPM (Statistical Parametric Mapping). https://www.fil.ion.ucl.ac.uk/spm-statistical-parametric-mapping/. Published January 14, 2020. Accessed April 5, 2024.

11. Gaser C, Dahnke R, Thompson PM, Kurth F, Luders E, Alzheimer's Disease Neuroimaging Initiative. CAT – A Computational Anatomy Toolbox for the Analysis of Structural MRI Data. June 2022. doi:10.1101/2022.06.11.495736

12. Yotter RA, Dahnke R, Thompson PM, Gaser C. Topological correction of brain surface meshes using spherical harmonics. *Hum Brain Mapp*. 2011;32(7):1109-1124. doi:10.1002/hbm.21095

13. Dahnke R, Yotter RA, Gaser C. Cortical thickness and central surface estimation. *NeuroImage*. 2013;65:336-348. doi:10.1016/j.neuroimage.2012.09.050

14. Computational Anatomy Toolbox CAT12. https://neuro-jena.github.io/cat12-help/.

15. Consolini J, Demirci N, Fulwider A, Hutsler JJ, Holland MA. Bok's equi-volume principle: Translation, historical context, and a modern perspective. *Brain Multiphysics*. 2022;3:100057. doi:10.1016/j.brain.2022.100057

16. Dinse J, Härtwich N, Waehnert MD, et al. A cytoarchitecture-driven myelin model reveals area-specific signatures in human primary and secondary areas using ultra-high resolution in-vivo brain MRI. *NeuroImage*. 2015;114:71-87. doi:10.1016/j.neuroimage.2015.04.023

17. The Dutch National 14 Tesla MRI initiative in Medical Science (Dynamic), NWO. https://www.nwo.nl/en/projects/184036009. Accessed April 2, 2024.

18. U.S. Food and Drug FDA clears first 7T magnetic resonance imaging device, Administration. https://www.fda.gov/news-events/press-announcements/fda-clears-first-7t-magnetic-resonance-imaging-device. Accessed April 2, 2024.

19. Katscher U, Börnert P, Leussler C, van den Brink JS. Transmit SENSE. *Magn Reson Med*. 2003;49(1):144-150. doi:10.1002/mrm.10353

20. Zhu Y. Parallel excitation with an array of transmit coils. *Magnetic Resonance in Medicine*. 2004;51(4):775-784. doi:10.1002/mrm.20011

21. Marques JP, Gruetter R. New Developments and Applications of the MP2RAGE Sequence - Focusing the Contrast and High Spatial Resolution R1 Mapping. Yacoub E, ed. *PLoS ONE*. 2013;8(7):e69294. doi:10.1371/journal.pone.0069294

22. Weiskopf N, Suckling J, Williams G, et al. Quantitative multi-parameter mapping of R1, PD*, MT, and R2* at 3T: a multi-center validation. *Front Neurosci*. 2013;7. doi:10.3389/fnins.2013.00095

23. Olsson H, Andersen M, Kadhim M, Helms G. MP3RAGE: Simultaneous mapping of T_1 and B1+ in human brain at 7T. *Magnetic Resonance in Med*. 2022;87(6):2637-2649. doi:10.1002/mrm.29151

24. Haast RAM, Lau JC, Ivanov D, Menon RS, Uludağ K, Khan AR. Effects of MP2RAGE B1+ sensitivity on inter-site T1 reproducibility and hippocampal morphometry at 7T. *NeuroImage*. 2021;224:117373. doi:10.1016/j.neuroimage.2020.117373

25. Bapst B, Massire A, Mauconduit F, et al. Pushing MP2RAGE boundaries: Ultimate time-efficient parameterization combined with exhaustive T_1 synthetic contrasts. *Magnetic Resonance in Med*. 2024;91(4):1608-1624. doi:10.1002/mrm.29948

26. Forodighasemabadi A, Rasoanandrianina H, El Mendili MM, Guye M, Callot V. An optimized MP2RAGE sequence for studying both brain and cervical spinal cord in a single acquisition at 3T. *Magnetic Resonance Imaging*. 2021;84:18-26. doi:10.1016/j.mri.2021.08.011

Supporting information for the paper: *Tolerating B_1^+-inhomogeneity in MP2RAGE-based R_1-mapping by calculating second contrast that permits previously problematic sequence parameters.* Lenno Ruijters, Torben Ellegaard Lund, Mads Sloth Vinding

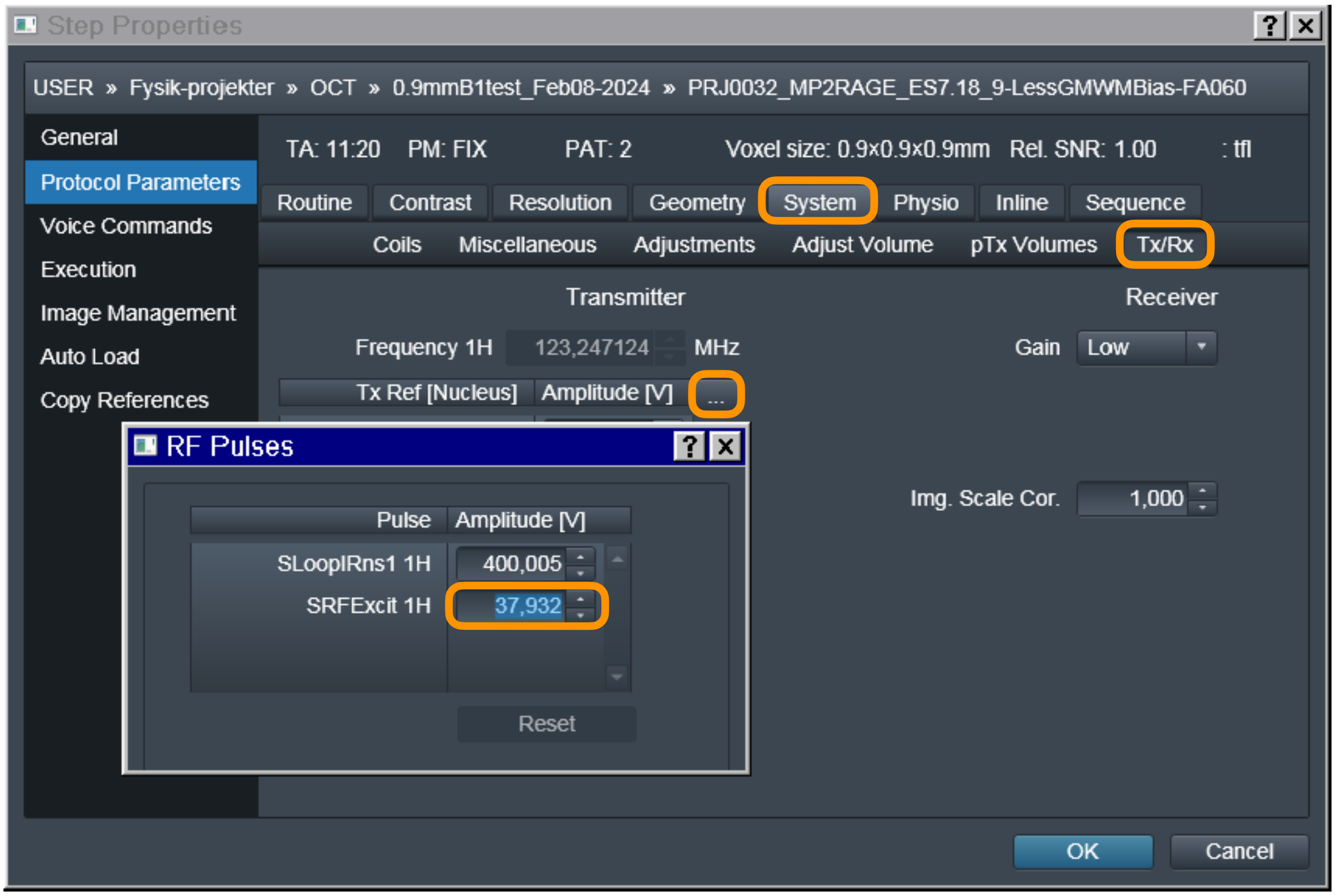

Supporting Figure S1: Screenshot of Syngo scan card user interface (Siemens Healthineers, Erlangen, Germany) showing in orange highlights where SRFExcit was modified.

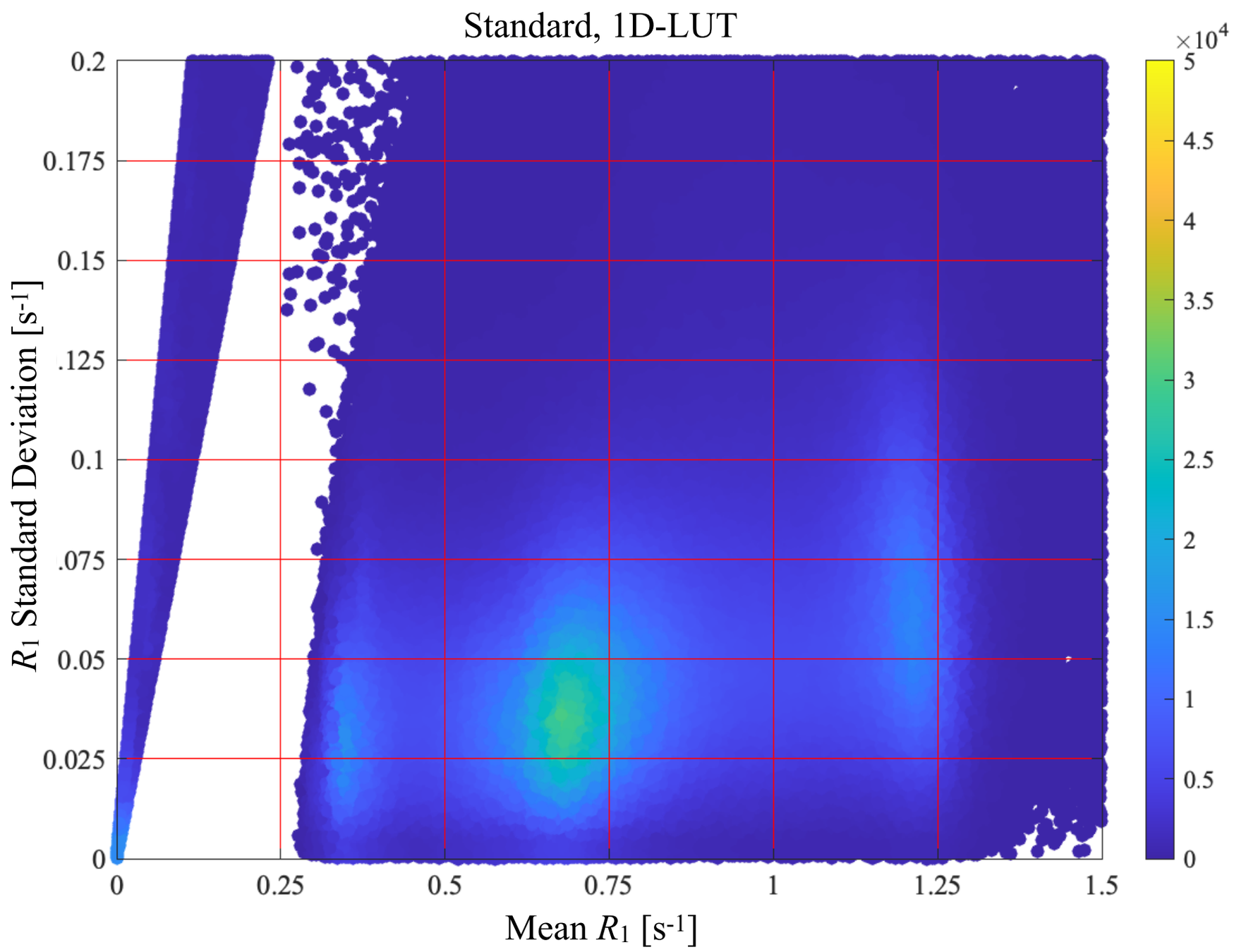

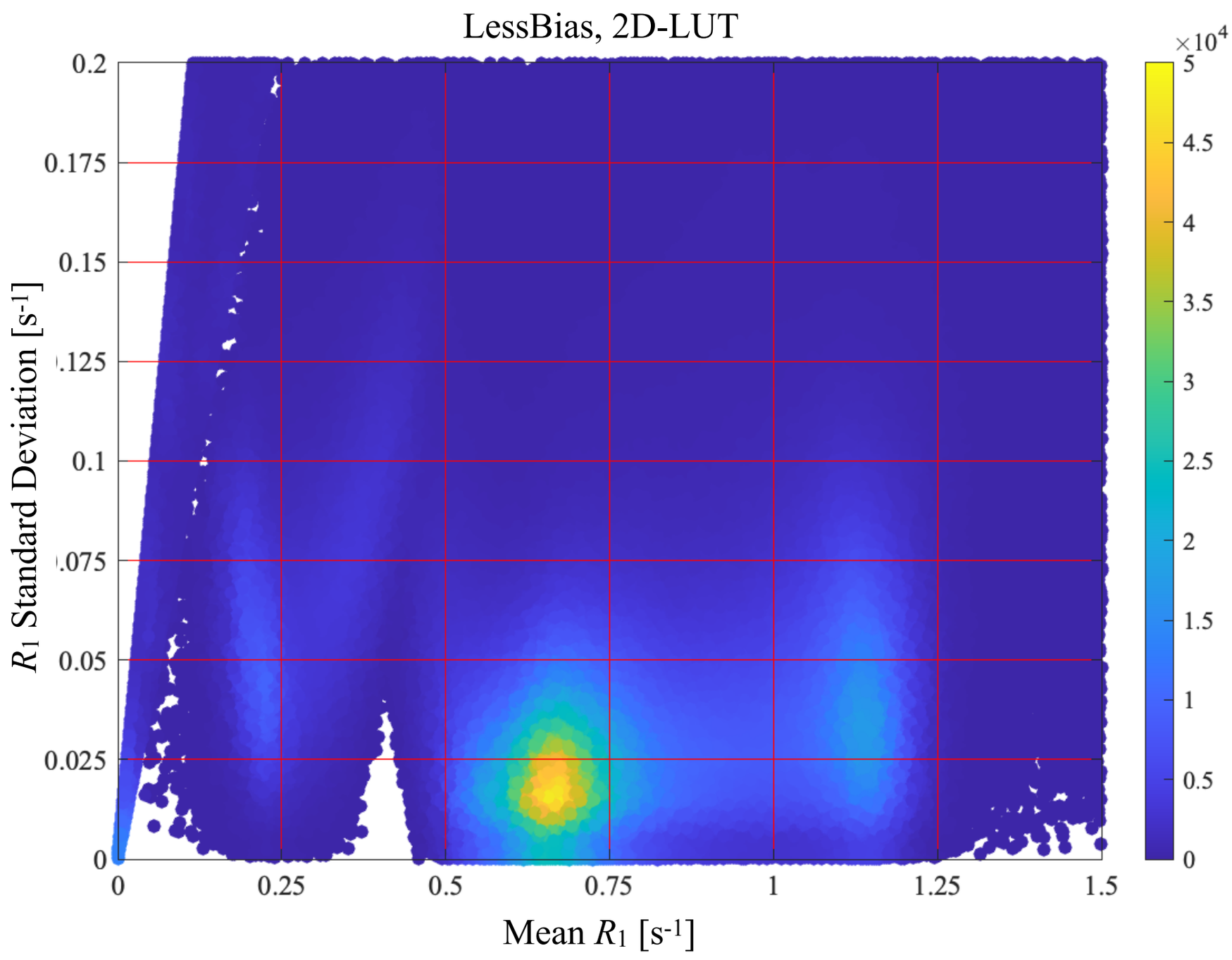

Supporting Figure S2: Distribution of voxel-wise standard deviations across excitation pulse scalings over the mean R_1 for the Standard (top) and LessBias (bottom) protocols. Increased density of the distribution is seen for and $R_1 \approx 0.7$ s^{-1} (GM) and $R_1 \approx 1.15$ s^{-1} (WM) at lower standard deviations in LessBias compared to Standard, suggesting higher consistency across the R_1-estimations. Voids (white) in both distributions correspond with folds in the respective transfer curves ($R_1 < 0.26$ s^{1} in Standard; $R_1 \approx 0.1$ s^{-1} (fold in DSR) or $R_1 \approx 0.4$ s^{-1} (fold in UNI) in LessBias), indicating R_1-nulling.